nature materials

Article

https://doi.org/10.1038/s41563-023-01705-y

Anion optimization for bifunctional surface passivation in perovskite solar cells

Received: 24 January 2023

Accepted: 27 September 2023

Published online: 30 October 2023

Check for updates

Jian Xu[1,4], Hao Chen[1,4], Luke Grater[1,4], Cheng Liu[2], Yi Yang[2], Sam Teale[1], Aidan Maxwell[1], Suhas Mahesh[1], Haoyue Wan[1], Yuxin Chang[1], Bin Chen[1,2], Benjamin Rehl[1], So Min Park[1], Mercouri G. Kanatzidis[2] & Edward H. Sargent[1,2,3]

Pseudo-halide (PH) anion engineering has emerged as a surface passivation strategy of interest for perovskite-based optoelectronics; but until now, PH anions have led to insufficient defect passivation and thus to undesired deep impurity states. The size of the chemical space of PH anions (>10^6 molecules) has so far limited attempts to explore the full family of candidate molecules. We created a machine learning workflow to speed up the discovery process using full-density functional theory calculations for training the model. The physics-informed machine learning model allowed us to pinpoint promising molecules with a head group that prevents lattice distortion and anti-site defect formation, and a tail group optimized for strong attachment to the surface. We identified 15 potential bifunctional PH anions with the ability to passivate both donors and acceptors, and through experimentation, discovered that sodium thioglycolate was the most effective passivant. This strategy resulted in a power-conversion efficiency of 24.56% with a high open-circuit voltage of 1.19 volts (24.04% National Renewable Energy Lab-certified quasi-steady-state) in inverted perovskite solar cells. Encapsulated devices maintained 96% of their initial power-conversion energy during 900 hours of one-sun operation at the maximum power point.

The optoelectronic properties of metal halide perovskite materials have enabled rapid progress in solar cell efficiency[1]. Further increases in power-conversion efficiency (PCE) require improved open-circuit voltage (V_{OC}), as the short circuit current (J_{SC}) is now close to the Shockley–Queisser limit[2].

The V_{OC} of perovskite solar cells (PSCs) is curtailed by non-radiative recombination arising due to surface and interfacial trap states. In addition, these defects accelerate PSC degradation, facilitating rapid halide-ion migration[3] and chemical reactions with water, oxygen and light[4]. Generally, perovskite compounds have a chemical formula ABX_3, where 'A' is a monovalent cation, 'B' is a divalent cation and 'X' is a halide anion. Ammonium ligands (PEA^+, BA^+, F–PEA^+, among others)[5,6] are now widely employed for passivation (Supplementary Table 1). However, this A-site passivation technique commonly demands delicate control over the dimensionality of the two-dimensional layer making up the two-dimensional:three-dimensional heterostructure. Furthermore, associated ligand intercalation has been documented to lead to degradation[7,8].

More recently, the use of pseudo-halide (PH) anions for X-site passivation has gained attention as it avoids the formation of lower-dimensional phases. X-site defects are more deleterious than A-site defects, motivating a focus onto their passivation[9]. However, only a few PH anions have been reported to work well in PSCs[10–12], a trend that we posited could arise from inefficient passivation and the introduction of unwanted deep impurity states induced by PH anions. This led us to hypothesize that a full search of the associated chemical space could

[1]Department of Electrical and Computer Engineering, University of Toronto, Toronto, Ontario, Canada. [2]Department of Chemistry, Northwestern University, Evanston, IL, USA. [3]Department of Electrical and Computer Engineering, Northwestern University, Evanston, IL, USA. [4]These authors contributed equally: Jian Xu, Hao Chen, Luke Grater. e-mail: ted.sargent@utoronto.ca

potentially uncover new and effective passivants, and thus harness the passivation potential of this diverse class of molecules in PSCs.

We thus embarked on a systematic search for PH anions exhibiting strong binding to the perovskite surface, which we offer as a surrogate for the degree of passivation. To this, a further criterion was added: the anions should not introduce impurity states in the perovskites. Given the large chemical space, it would be impractical to rely on conventional trial-and-error. Instead we sought a route to study structure–property–performance relationships in a high throughput manner[13,14], seeking to understand how the PH anion's chemical structure influences its ability to passivate.

Workflow for materials screening

To accomplish this, we used density functional theory (DFT) on a subset of the chemical space and trained thusly a machine learning (ML) model (Fig. 1a). First we screened the PH space for experimentally reasonable candidates. A multistep screening funnel considered the charge state (tier 1), molecular weight (tier 2), availability of three-dimensional structures (tier 3), molecular radii (tier 4), presence of Na or K salts (tier 5), and salt purchase availability (tier 6). The rationale for specific threshold values used in the materials screening procedure are discussed in Supplementary Note 1 and Supplementary Fig. 1. Only 168 PH anions remained out of five million molecules derived from the PubChem database.

We investigated the interaction between PH anions and the perovskite surface (Fig. 1b) using $FA_{0.75}MA_{0.25}PbI_3$ as a model system for investigation. The PH anions can interact with the perovskite surface via substitution, wherein the PH anion replaces an X (I^-) atom; or via adsorption through binding with under-coordinated B^{2+} (Pb^{2+}) cations. From formation energies ($\Delta E_{formation}$) (Fig. 1c), we find that substitution is more thermodynamically favourable than adsorption in most I chemical potential ($\Delta\mu_I$) regions. This is attributed to the formation of more ionic bonds between Pb^{2+} and the electron-rich group of PH anions, as well as more hydrogen bonds between NH_3^+ group of FA^+/MA^+ and PH anions. The charge density difference reveals charge transfer between PH anions at the surface and the perovskite slab, indicating that PH anions could attract electrons from neighbouring Pb and MA/FA atoms (Supplementary Fig. 2).

In light of this understanding of the PH anion passivation mechanism, we performed DFT calculations to obtain estimates for the binding energies (E_b) (Supplementary Fig. 3) of PH anions with the perovskite surface. As shown in Fig. 2a, several new PH anions have even higher E_b than the 16 anions studied in earlier literature. The calculated E_b trends in $FA_{0.75}MA_{0.25}PbI_3$ appear to extend well to other perovskite compositions, for example, $FA_{0.75}Cs_{0.25}PbI_3$ (normal bandgap), $FA_{0.75}MA_{0.25}Pb_{0.5}Sn_{0.5}I_3$ (narrow bandgap) and $FA_{0.75}Cs_{0.25}Pb(I_{0.625}Br_{0.375})_3$ (wide bandgap), as seen in Supplementary Fig. 4. Since higher E_b indicates stronger binding strength to iodine vacancies, V_I, we expect these candidates to offer enhanced passivation.

Machine-learning-model training and analysis

We then sought to develop a physics-informed machine learning (ML) model to investigate how the molecular structure of PH anions regulates their interaction strength with the perovskite surface. Screened PH anions have diverse electron-rich functional groups, including $R–SO_3^-$, $R–SO_2^-$, $R–CO_2^-$, $R–COS^-$, $R–S_2O_2^-$, $R–CS_2^-$, $R–BF_3^-$, PO_3^-, $R–PO_2^-$, $R–PHO_3^-$, $R–S^-$, $R–O^-$. Jeong et al. reported that the PH anion, formate ($HCOO^-$), had a binding energy of 3.1 eV, resulting in record-performing *n-i-p* (negative-intrinsic-positive) PSCs, while chloride (Cl^-) had a binding energy of 2.98 eV (ref. 10). In light of this, we used 3 eV as a basis to classify 267 PH anions, including our 168 screened p-h anions (Fig. 1a), into high/low E_b: thus the PH anions are either labelled as higher E_b (201 anions) or as lower E_b (66 anions), and these are taken as the ML outputs. As shown in Fig. 2b, we initially considered 19 features of the PH anions as ML inputs (see Methods for ML details).

After two rounds of ML training, we identify four primary features that influence the E_b classification, including the number of oxygen atoms (num_O), topological polar surface area (TPSA), hydrogen bond acceptor count (HBA) and highest occupied molecular orbital levels (HOMO). Using these four features, we achieve a receiver operating characteristic (ROC) area under curve (AUC) score of 0.87 and an accuracy score of 0.84 in the random forest model (Fig. 2c, top panel, and Supplementary Fig. 5). In the logistic regression model, features with positive coefficients are beneficial for the positive label ('higher E_b' class) (Fig. 2c and Supplementary Figs. 6 and 7). We thus provide a set of guidelines for the binding energy determination: PH anions with more num_O, larger TPSA, more HBA and lower HOMO levels tend to exhibit stronger binding strength with the perovskite surface.

Physically, a higher num_O provides more active sites to interact with Pb^{2+} at the perovskite surface via coordination bonding. For example, we found that PH anions with SO_3^- functional groups at the head-side tend to have higher binding energy than those with CO_2^- functional groups. More HBA, defined as the sum of atoms in the molecule that contain lone electron pairs participating in the hydrogen bonding[15], indicates increased likelihood to form hydrogen bonds between PH anions and the NH_3^+ group of FA^+/MA. TPSA is also linked to the hydrogen bonding (both donor and acceptor groups)[15]. The HOMO levels are mostly situated on the electron-rich side, as shown by the red electrostatic potential (ESP) regions (Fig. 2b). Lower HOMO levels usually indicate a higher electronegativity[16,17], resulting in stronger electrostatic interaction between the PH anion and a positively charged defect (for example, V_I) on the perovskite surface. Thus, when we progress I^-, Br^-, Cl^-, to F^-, the increased electronegativity is accompanied by decreased *p*-orbital energy levels, and stronger E_b (Fig. 2a).

Bifunctional defect passivation mechanism

We also sought to prevent deep impurity states caused by the PH treatment itself, as they increase non-radiative losses. This prompted us to look for safe functional groups: in the higher E_b class ($E_b > 3$ eV), we identify 24 potential PH anions (Figs. 2a and 3d) that did not produce localized states near the band edges, regardless of the calculation method level used (see detailed electronic structures in Supplementary Figs. 8–10 and Supplementary Note 2).

The candidate molecules that emerged prompted us to look at the effect of functional groups on the formation of I_{Pb} anti-site defects (Fig. 3a), known to lead to deep levels within the bandgap in (MA/FA)PbI_3 perovskites[18,19]. We found that SO_3^- functional groups cause greater surface-structure distortion that inhibits the passivation of negatively charged I_{Pb} anti-site defects, while CO_2^- prevents the formation of I_{Pb}—but, as previously noted, has a lower surface binding strength.

To overcome this undesirable trade-off, we explored bifunctional ligands: a head group (electron-rich side) with less surface-structure distortion and anti-site defect generation; and a tail (electron-poor side) engineered to increase binding affinity. In this work, we defined 'bifunctional passivation' as the ability to passivate both positively charged and negatively charged defects at perovskite surface. Specifically, the CO_2^- functional group seemed a good choice for the head-side, providing less steric hindrance and reduced distortion; and either chalcogen- or halogen-containing functional groups for the tail to increase binding affinity. To evaluate candidate tail groups, we calculated the integrated crystal orbital Hamilton population (ICOHP)[20], a measure of bonding strength. As shown in Fig. 3b, we found that those with the S atom at the tail-side forms a stronger coordination bond with Pb^{2+} than do the other candidates (for example, O–Pb, Cl–Pb and F–Pb). A stronger bond suggests it would cost more energy to break the initial bonding to create I_{Pb} defects. Therefore, it appears that bifunctional PH anions can simultaneously fill donor-like defects V_I, while also passivating acceptor-like defects (I_{Pb}). As shown in Fig. 3a, there are 15 PH anions having defect formation energies ΔE_f (I_{Pb}) > 0, which are considered as bifunctional ligands.

https://doi.org/10.1038/s41563-023-01705-y

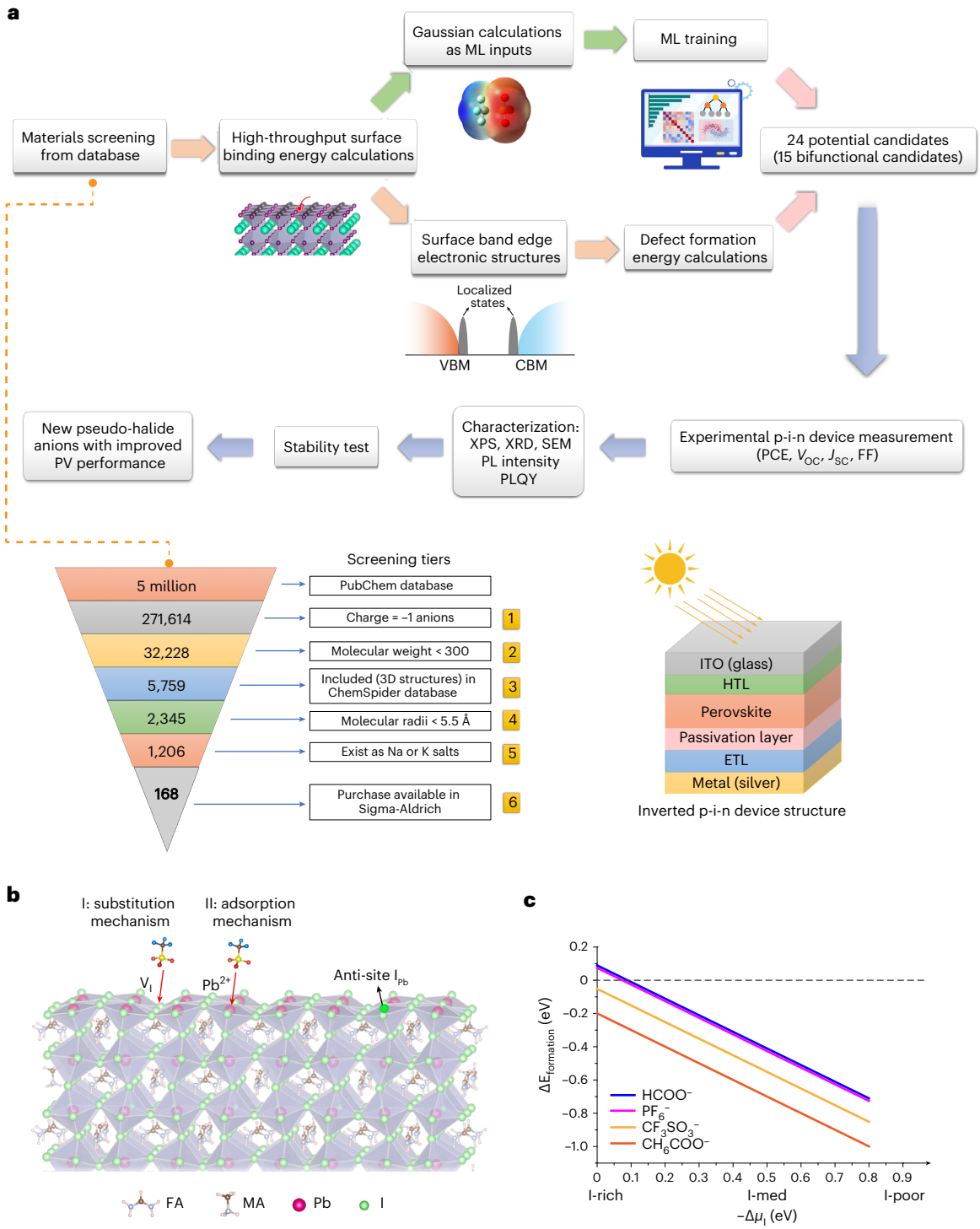

Fig. 1 | Workflow to identify candidate PH anions as passivants to improve PV performance in PSCs. a, Material screening process workflow with six screening tiers.VBM, valence band maximum; CBM, conduction band minimum. **b**, Schematic of the interaction between PH anions with the perovskite surface. **c**, Formation energies ($\Delta E_{formation}$) of the substitution versus adsorption mechanisms, as a function of the iodine chemical potential. The $E_{formation}$ of the adsorption mechanism was set as the reference (zero). 3D, three-dimensional.

We also sought to calculate the anion migration barrier (ΔE_a) at the perovskite surface, as halide migration is one cause of current–voltage hysteresis and decomposition of perovskite films[3]. As shown in Fig. 3c and Supplementary Fig. 11, ΔE_a for I^- (vacancy mediated) is 0.23 eV (averaged), consistent with previous calculation results[21]. We find that Br^-, Cl^- and F^- have an increased ΔE_a of 0.27 eV, 0.32 eV and 0.37 eV, linked to enhanced electronegativity and binding strength with the perovskite surface (Fig. 2a). The optimal bifunctional PH anions (ligand **14**) further increase the ΔE_a to 0.43 eV, the result of enhanced binding strength and the additional PH anion, FA^+/MA^+ molecular rotation barrier, the latter absent in halide (I^-, Br^-, Cl^-) migration.

Photovoltaic performance of PSCs

Experimentally, we took five bifunctional PH anions with higher E_b for further investigation. We dissolved PH anion salts in a solution of isopropanol (IPA), which we spin coated on perovskite films at 0.5 mg ml^{-1}

https://doi.org/10.1038/s41563-023-01705-y

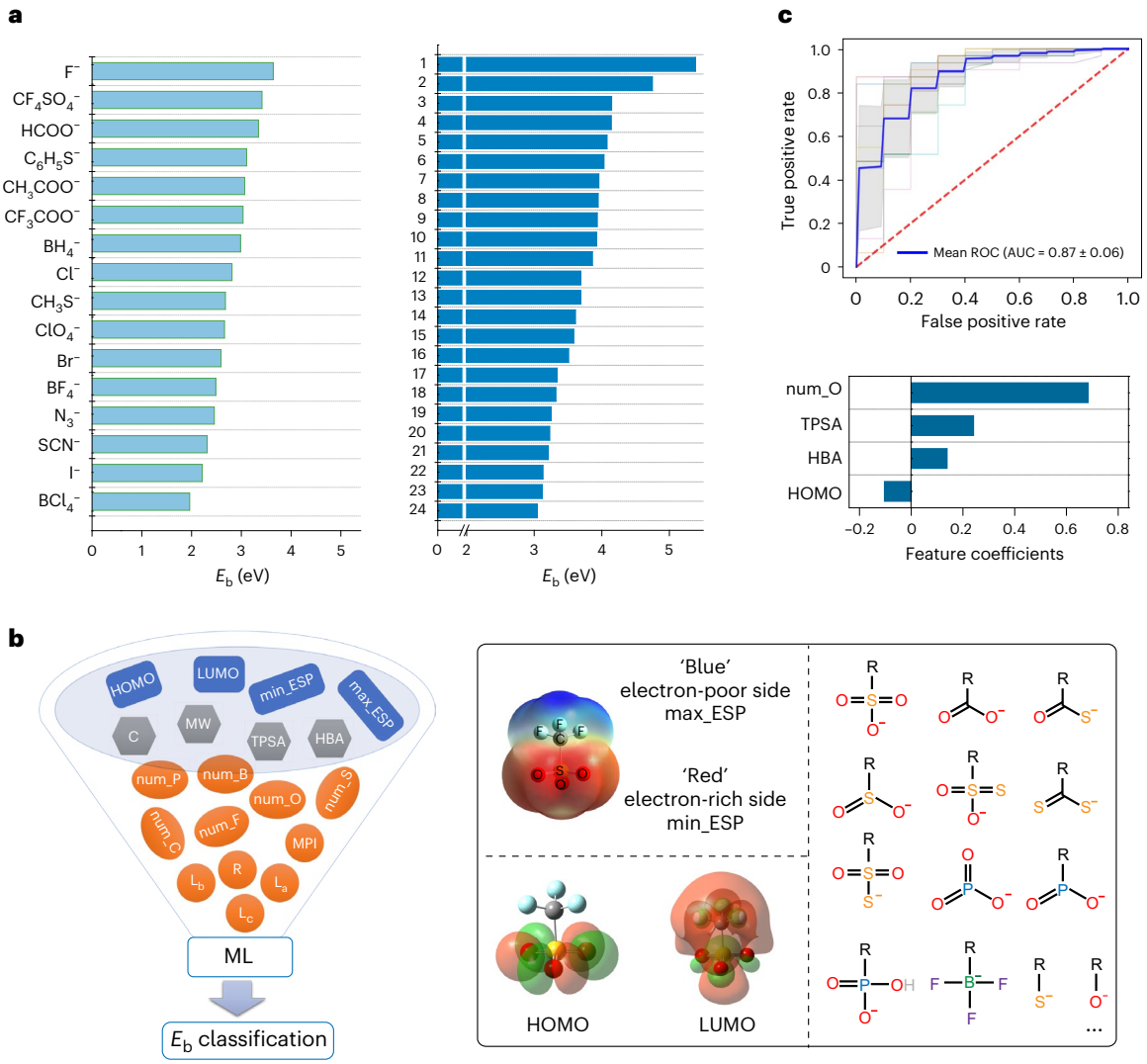

Fig. 2 | Determination of the ranking and chemical role of physical features that dominate binding energy performance of candidate PH anions. **a**, DFT-calculated E_b of different anions with V_I at the perovskite surface. Sixteen previously reported anions (left) and 24 unreported PH anions (right) with $E_b > 3$ eV that do not create trap states on the perovskite surface are shown. **b**, Nineteen features as ML inputs. ESP and functional group type of the electron-rich side of PH anions are shown in the right panel. **c**, ML training results: ROC curve from the random forest model and feature coefficients generated from the logistic regression model are shown in the top and bottom panels, respectively. AUC = $\mu \pm \sigma$, where μ and σ are the average and standard deviation of the ten-fold ROC AUC scores.

(Supplementary Fig. 12) and then annealed at 100 °C (Methods). We then fabricated inverted PSC devices without and with PH anion treatments (Fig. 4a). We employed $Cs_{0.05}FA_{0.9}MA_{0.05}Pb(I_{0.95}Br_{0.05})_3$ perovskite with a bandgap of 1.55 eV as the absorber. The PSCs had an inverted device architecture of ITO/NiO_x/Me–4PACz/perovskite/C_{60}/BCP/Ag, where ITO is indium tin oxide, Me–4PACz is [4-(3,6-dimethyl-9H-carbazol-9-yl)butyl]phosphonic acid, C_{60} is fullerene and BCP is bathocuproine. In PSCs with an inverted (*p-i-n*) device structure, the interface between the perovskite layer and the electron transport layer (ETL) has been proven to be the most crucial to device performance due to substantial interfacial non-radiative recombination[22,23]. This motivated us to focus on the use of a PH anion passivation layer at the perovskite/ETL interface.

Figure 4b shows the current density–voltage (*J–V*) curves for control versus five PH anion-treated devices under forward and reverse scanning. It reveals that sodium thioglycolate (ST) performed the best, though all five PH anions showed improved performance over controls. This we attributed to the optimal bifunctional passivation effect of thioglycolate. Both control and PH anion-treated devices exhibit low hysteresis. Figure 4c shows device performance statistics using five different PH anion treatments (ST (ligand **14**); sodium chlorate (SC) (ligand **2**); potassium bicarbonate (PB) (ligand **7**); sodium hydroxyacetate (SH) (ligand **13**); and monosodium methylphosphonate (MMP) (ligand **12**)). We found that the V_{OC} and PCE of these five PH anion-treated devices followed the order: ST best, SC worst, and SH, MMP and PB were in between. This sequence is consistent with the order of the calculated ΔE_f (I_{Pb}) of Fig. 3a: ST > SH > MMP > PB > SC. The role of sodium was discussed in Supplementary Note 3 and Supplementary Figs. 13 and 14.

In ST-treated devices, V_{OC} and the fill factor (FF) were the basis of the improvement, with J_{SC} remaining effectively unchanged. V_{OC} improved from 1.14 V in control to 1.19 V in ST-treated devices and FF increased from 81.9% to 83.6% (see detailed photovoltaic (PV) parameters in Fig. 4b). The ST-treated devices had a considerably higher stabilized power output of 24.2% compared with 22.5% for the controls (Supplementary Fig. 15). External quantum efficiency spectra (Supplementary Fig. 16) verified the J_{SC} values obtained from the *J–V*

https://doi.org/10.1038/s41563-023-01705-y

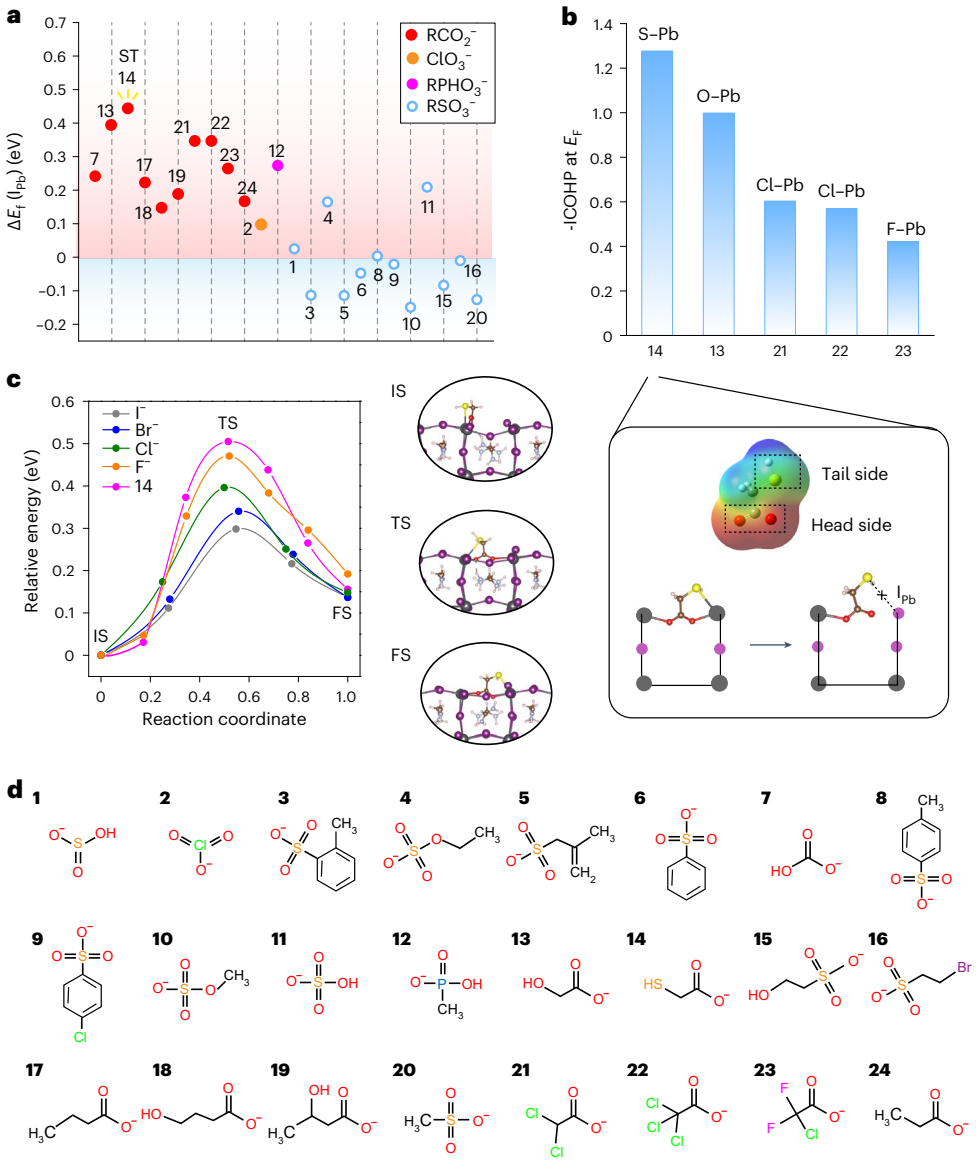

Fig. 3 | Computational studies of bifunctional ligand candidates. a, Defect formation energies (ΔE_f) of I_{Pb} anti-site defects when PH anions are substituted at the V_I site. The values in the I^- case were set to zero for comparison. Sodium thioglycolate (ST) was the most effective passivator. The numbers next to the data points correspond to the assigned number for each PH anion. **b**, The negative of ICOHP (-ICOHP) at the Fermi level (E_F) for X–Pb bonding (X = S/O/Cl/F) for ligands **13**, **14**, **21**, **22** and **23** adsorbed perovskite surfaces. **c**, Energy profile and migration barrier for I^-/Br^-/Cl^-/F^-/ligand **14** migration on the perovskite surface. Atomic configurations (initial state (IS), transition state (TS) and final state (FS)) of ligand **14** migrations along the migration pathways are shown. **d**, Molecular structures of the 24 potential PH anions. These are labelled **1**–**24** in the same manner as in Fig. 2a. S atoms, yellow; O atoms, red; Pb atoms, grey; I atoms, purple.

measurements. We fabricated 15 ST-treated PSCs and the narrow PCE distribution indicates good reproducibility (statistics in Fig. 4c). An ST-treated device was certified at an independent institute, National Renewable Energy Lab, and achieved a quasi-steady-state PCE of 24.04% (V_{OC} = 1.16 V, J_{SC} = 25.12 mA cm^{-2} and FF = 82.48%) (Supplementary Fig. 17). This efficiency ranks amongst the best reported in the literature for inverted PSCs (Supplementary Table 1).

Next, we sought to characterize the morphology and crystallinity of the perovskite films to reveal the interaction between the perovskite and the PH anion treatments. Top down and cross-sectional scanning electron microscopy (SEM) images show that the film morphology remains unchanged after the PH anion treatments (Supplementary Figs. 13 and 20). The PH anion treatments did not affect overall crystallinity and perovskite phase, with no erroneous peaks, and lack of correlative peak shifting, broadening, or intensity differences, as evidenced by indexed thin-film and simulated X-ray diffraction (XRD) patterns (Supplementary Figs. 18 and 19). Additionally, ST and MMP treatments are found to reduce excess PbI_2, an added benefit for stability (Fig. 5a and Supplementary Fig. 18). The impact of posttreatment recrystallization on the morphology of perovskite thin films was discussed in Supplementary Note 4 and Supplementary Figs. 20 and 21.

To ascertain whether our top performing PH anion (thioglycolate) was present following posttreatment, we used X-ray photoelectron spectroscopy (XPS), whose O 1*s* peak (Fig. 5b) and S 2*p* peak (Fig. 5c) suggest that PH anions anchor at the perovskite film surface. Upon ST treatment, a binding energy shift of 0.24 eV and 0.34 eV was observed for the Pb $4f_{5/2}$ and Pb $4f_{7/2}$ orbitals, respectively, indicating a strong interaction between the PH anion and the perovskite surface (Fig. 5d).

https://doi.org/10.1038/s41563-023-01705-y

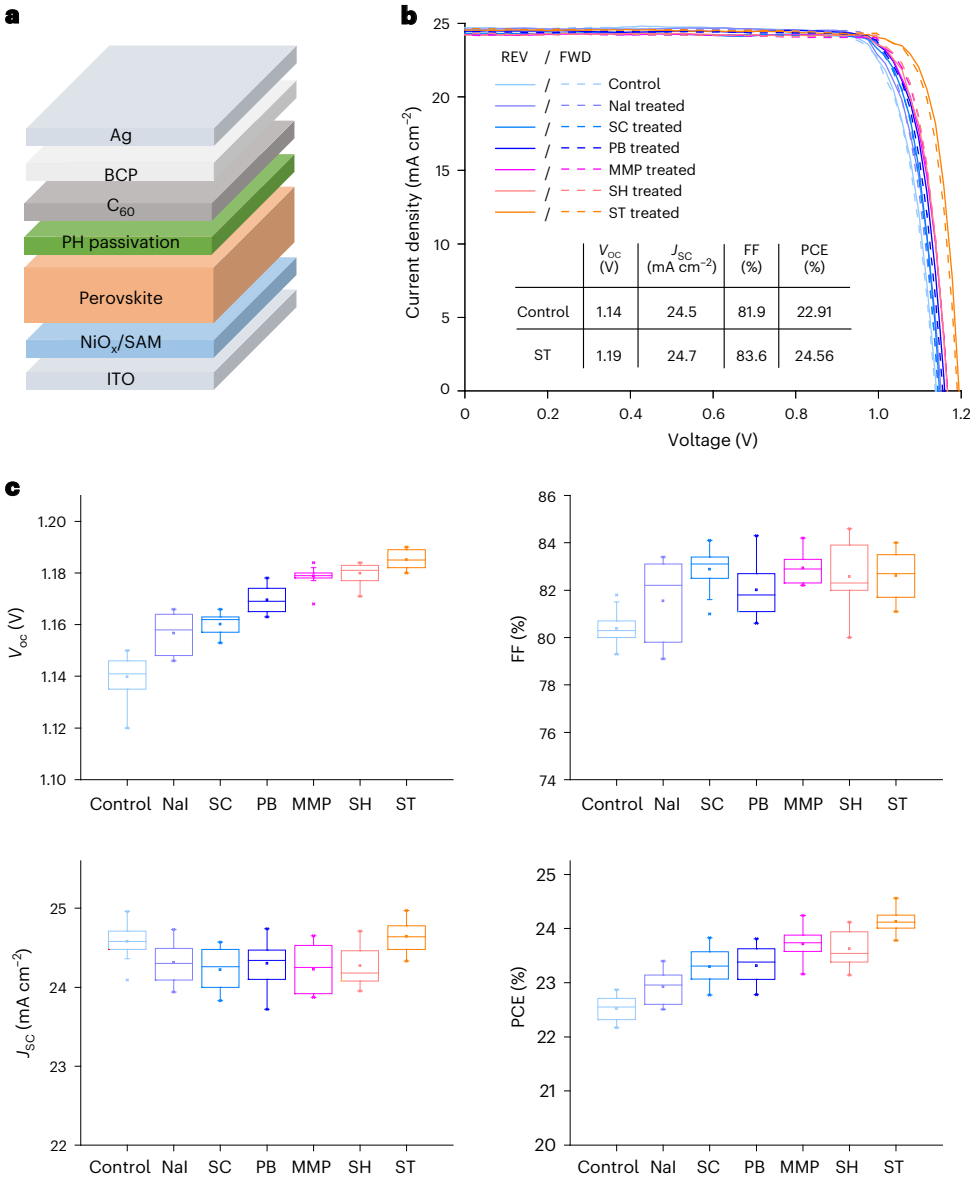

Fig. 4 | Experimental study of device performance in PH anion-treated devices compared to relevant controls. a, Inverted perovskite solar cell architecture. **b**, *J*–*V* scans of the control, NaI and five PH anion-treated devices (ST (ligand **14**); SC (ligand **2**); PB (ligand **7**); SH (ligand **13**); MMP (ligand **12**)). **c**, Comparison of PV performance among control, NaI and five PH anion-treated PSCs (aperture area, 0.049 cm^2) processed in the same runs (15 devices for each type). The box plot denotes minima (bottom line), maxima (top line), median (centre line), and 75th (top edge of the box) and 25th (bottom edge of the box) percentiles. REV, reverse scan; FWD, forward scan.

We provide detailed C, S, Pb, O, Na, N, I and Cs XPS spectra for all five PH anions (ST, SH, MMP, PB and SC) in Supplementary Fig. 22. In addition, we performed sputtering XPS (Methods) on control and ST-treated samples to evaluate the penetration depth of the PH treatment (Supplementary Fig. 23) and our results indicate that the thioglycolate anion remained within 5 nm of the perovskite surface, as evidenced by the S 2*p* peak (Supplementary Note 5).

To investigate if the thioglycolate treatment leads to defect passivation, we compared the steady-state photoluminescence (PL) of control and ST-treated films. For the PL measurements, we used a glass/perovskite/PH treatment architecture. The PL emission intensity of the ST-treated film was more than three times higher than that of the control sample (Fig. 5e), indicating that the PH anion treatment reduces non-radiative recombination in perovskite films. The photoluminescence quantum yield (PLQY), on average, increased from 20% to 44% upon ST treatment (Supplementary Fig. 24), while the remaining PH treatments all exhibited a higher average PLQY over the control (Supplementary Fig. 14). We anticipated that the average bulk quasi-Fermi level splitting (QFLS) will rise from 1.23 to 1.26 eV after ST treatment (Methods). The V_{OC} increase (from 1.14 V to 1.19 V) in ST-treated devices is consistent with their increased PLQY. Furthermore, applying the ST PH treatment to a different perovskite composition, namely a narrow-bandgap $Cs_{0.05}FA_{0.7}MA_{0.25}Pb_{0.5}Sn_{0.5}I_3$, was found to result in the highest PLQY over the control and other PH anions (Supplementary Fig. 25), hinting at wider applicability of bifunctional PH anions.

We investigated the long-term operational stability of ST-treated PSC devices under 1-sun-equivalent light-emitting diode (LED) illumination after confirming sufficient longevity under AM1.5 G standards (Supplementary Note 6 and Supplementary Fig. 26). These encapsulated devices were biased with fixed resistance loads near the maximum power point (MPP). The ST-treated device retains 96% of its initial PCE after a period of 900 hours (Fig. 5f and Supplementary Fig. 27).

https://doi.org/10.1038/s41563-023-01705-y

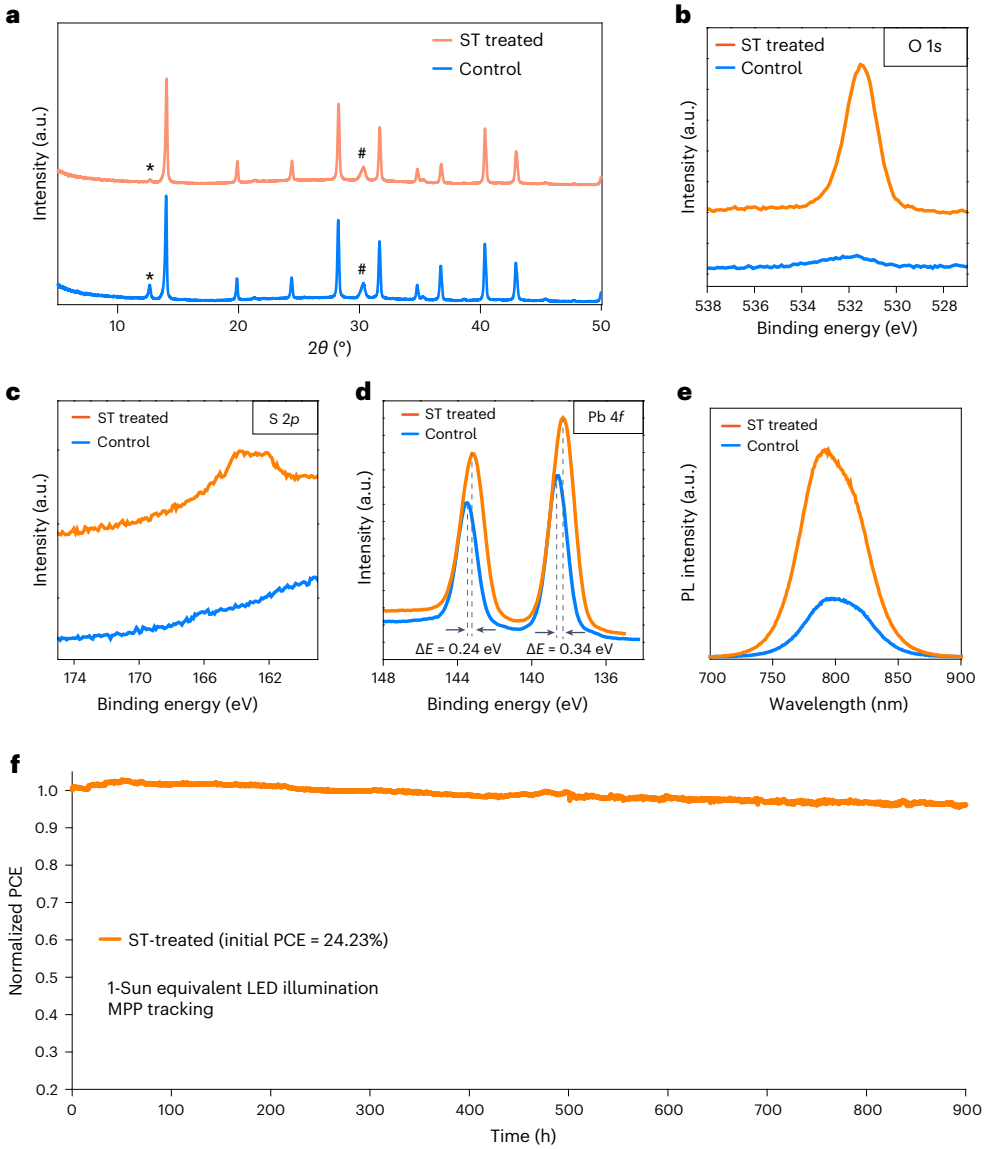

Fig. 5 | Experimental characterization of ST-treated perovskite films and device stability. a, XRD patterns of control and ST-treated perovskite films. The symbols of * and # represent the PbI_2 peak and ITO peak, respectively. **b**, XPS spectra of O 1*s* of control and ST-treated films. **c**, XPS spectra of S 2*p* of control and ST-treated films. **d**, XPS spectra of Pb 4*f* of control and ST-treated films. **e**, Steady-state PL spectra of control and ST-treated perovskite films. **f**, MPP tracking of ST-treated devices using 1-sun-equivalent LED illumination. The operating temperature of the device was approximately 35 °C, and the relative humidity was approximately 30–40%.

The loss in PCE is primarily due to a decrease in current density, whereas the voltage showed little degradation (Supplementary Figs. 28 and 29). The MPP tracking findings are consistent with a picture of mitigated ion migration at the perovskite surface (Fig. 3c) and the reduction of PbI_2 in thin-film XRD (Fig. 5a).

The present study suggests that continued progress in combined computational, ML and experimental efforts has further potential for the discovery of molecular strategies to increase performance in optoelectronics, including photovoltaics, as well as in related light-emitting devices.

Online content

Any methods, additional references, Nature Portfolio reporting summaries, source data, extended data, supplementary information, acknowledgements, peer review information; details of author contributions and competing interests; and statements of data and code availability are available at https://doi.org/10.1038/s41563-023-01705-y.

References

1. Best Research-Cell Efficiencies. *National Renewable Energy Laboratory* https://www.nrel.gov/pv/cell-efficiency.html (publication date: July 10th, 2023).
2. Jiang, Q. et al. Surface passivation of perovskite film for efficient solar cells. *Nat. Photonics* **13**, 460–466 (2019).
3. Bi, E., Song, Z., Li, C., Wu, Z. & Yan, Y. Mitigating ion migration in perovskite solar cells. *Trends Chem.* **3**, 575–588 (2021).
4. Siegler, T. D. et al. Water-accelerated photooxidation of $CH_3NH_3PbI_3$ perovskite. *J. Am. Chem. Soc.* **144**, 5552–5561 (2022).
5. Wang, Z. et al. Efficient ambient-air-stable solar cells with 2D–3D heterostructured butylammonium-caesium-formamidinium lead halide perovskites. *Nat. Energy* **2**, 17135 (2017).
6. Chen, C. et al. Arylammonium-assisted reduction of the open-circuit voltage deficit in wide-bandgap perovskite solar cells: the role of suppressed ion migration. *ACS Energy Lett.* **5**, 2560–2568 (2020).

7. Chen, H. et al. Quantum-size-tuned heterostructures enable efficient and stable inverted perovskite solar cells. *Nat. Photonics* **16**, 352 (2022).
8. Azmi, R. et al. Damp heat-stable perovskite solar cells with tailored-dimensionality 2D/3D heterojunctions. *Science* **376**, 73–77 (2022).
9. Chen, B., Rudd, P. N., Yang, S., Yuan, Y. & Huang, J. Imperfections and their passivation in halide perovskite solar cells. *Chem. Soc. Rev.* **48**, 3842–3867 (2019).
10. Jeong, J. et al. Pseudo-halide anion engineering for α-$FAPbI_3$ perovskite solar cells. *Nature* **592**, 381–385 (2021).
11. Bu, T. et al. Lead halide–templated crystallization of methylamine-free perovskite for efficient photovoltaic modules. *Science* **372**, 1327–1332 (2021).
12. Chen, R. et al. Sulfonate-assisted surface iodide management for high-performance perovskite solar cells and modules. *J. Am. Chem. Soc.* **143**, 10624–10632 (2021).
13. Zhou, Y., Herz, L. M., Jen, A. K. Y. & Saliba, M. Advances and challenges in understanding the microscopic structure–property–performance relationship in perovskite solar cells. *Nat. Energy* **7**, 794–807 (2022).
14. Yao, Z. et al. Machine learning for a sustainable energy future. *Nat. Rev. Mat.* **8**, 202–215 (2023).
15. Veber, D. F. et al. Molecular properties that influence the oral bioavailability of drug candidates. *J. Med. Chem.* **45**, 2615–2623 (2002).
16. Goodson, F. S. et al. Tunable electronic interactions between anions and perylenediimide. *Org. Biomol. Chem.* **11**, 4797–4803 (2013).
17. Sun, C. et al. Hard and soft Lewis-base behavior for efficient and stable $CsPbBr_3$ perovskite light-emitting diodes. *Nanophotonics* **10**, 2157–2166 (2021).
18. Zhang, X., Shen, J. X., Turiansky, M. E. & Van de Walle, C. G. Minimizing hydrogen vacancies to enable highly efficient hybrid perovskites. *Nat. Mater.* **20**, 971–976 (2021).
19. Meggiolaro, D. & De Angelis, F. First-principles modeling of defects in lead halide perovskites: Best practices and open issues. *ACS Energy Lett.* **3**, 2206–2222 (2018).
20. Deringer, V. L., Tchougreeff, A. L. & Dronskowski, R. Crystal orbital Hamilton population (COHP) analysis as projected from plane-wave basis sets. *J. Phys. Chem. A* **115**, 5461–5456 (2011).
21. Yang, J.-H., Yin, W.-J., Park, J.-S. & Wei, S.-H. Fast self-diffusion of ions in $CH_3NH_3PbI_3$: the interstiticaly mechanism versus vacancy-assisted mechanism. *J. Mater. Chem. A* **4**, 13105–13112 (2016).
22. Warby, J. et al. Understanding performance limiting interfacial recombination in pin perovskite solar cells. *Adv. Energy Mater.* **12**, 2103567 (2022).
23. Chen, H. et al. Regulating surface potential maximizes voltage in all-perovskite tandems. *Nature* **613**, 676–681 (2023).

Methods

Computational details

We used the Vienna Ab initio Simulation Package (VASP)[24] to perform DFT-based first-principles calculations. The Perdew–Burke–Ernzerhof functional[25] and the screened Heyd–Scuseria–Ernzerhof hybrid functional[26,27] were used for the exchange-correlation functional. DFT-D3 method was used for the van der Waals correction[28]. The spin orbital coupling (SOC) effect was included in electronic structure calculations. In Heyd–Scuseria–Ernzerhof + spin orbital coupling calculations, the mixing parameter (α) of the Hartree–Fock term was set to 0.45, which had been proven to reproduce the experimental bandgap. We used the cutoff energy of 400 eV with the energy and force convergence tolerance setting to 10^{-5} eV and 0.03 eV Å^{-1}, respectively. The Brillouin zone was sampled with Γ-centred *k*-mesh densities of $2\pi \times 0.04$ Å^{-1}.

For the chemical bond analysis, we used the LOBSTER program[29] to calculate the ICOHP[20], a quantitative measure of bond strength. We employed Climbing Image Nudged Elastic Band method[30] to calculate the ion migration barrier (ΔE_a) at the perovskite surface.

Machine learning

We initially considered 19 features of PH anions as ML inputs: (1) electronic parameters calculated by Gaussian such as lowest unoccupied molecular orbital, HOMO, minimum electrostatic potential and maximum electrostatic potential; (2) structural parameters such as ionic radius (R), length (L_a), breadths (L_b), heights (L_c), molecular polarity index (MPI) and number of elemental species (num_O, num_S, num_F, num_P, num_B, num_C); and (3) fundamental parameters obtained from the Pubchem database such as molecular weight, TPSA, HBA and complexity. We obtained the data of lowest unoccupied molecular orbital, HOMO, minimum electrostatic potential, maximum electrostatic potential, R, L_a, L_b, L_c and MPI by postprocessing using the Multiwfn software[31].

As evidenced by the correlation matrix of continuous features (Supplementary Fig. 30), we abandon two highly correlated features (MPI and L_a) in the first-round ML training. On the basis of input features, we trained and evaluated five different classification ML models, including the random forest model, the gradient boosting classifier model, the XGboost model, the logistic regression model and the support-vector classifier model. The motivations behind choosing classification over regression were discussed in Supplementary Note 7 and Supplementary Fig. 31. We set aside 15% of the dataset as a test set, with the rest used as the training set. To avoid overfitting, we selected the ML model hyperparameter using StratifiedShuffleSplit with n_splits = 10 for cross-validation. We also considered regularization in the logistic regression model. We used the ROC AUC score and accuracy score as the evaluation metrics. As listed in Supplementary Table 2, the difference in ROC AUC and accuracy scores between the training and test tests was small, indicating a low likelihood of overfitting. We used the codes from Guo et al. to plot the ROC curves[32].

Materials

All materials were used as received without further purification. The organic halide salts (FAI, MABr) were purchased from GreatCell Solar Materials. PbI_2 (99.99%), $PbBr_2$ (99.999%) and [4-(3,6-dimethyl-9H-carbazol-9-yl)butyl]phosphonic acid (Me–4PACz) were purchased from TCI Chemicals. CsI (99.999%), SC, PB, SH, ST, MMP and nickel nitrate hexahydrate were purchased from Sigma–Aldrich. C_{60}, Bathocuproine (BCP) were purchased from Xi'an Polymer Light Technology Corp. All the solvents used in the process were anhydrous and purchased from Sigma–Aldrich.

Perovskite film and device fabrication

NiO_x nanocrystal (10 mg ml^{-1}) layers were first spin coated on ITO substrates at 3,000 r.p.m. for 25 s in air without any posttreatment, then the substrates were immediately transferred to the glovebox. The NiO_x nanoparticles were synthesized via the hydrolysis reaction of nickel nitrate referring to our previous work[33]. Me–4PACz (0.3 mg ml^{-1}) in ethanol was spin coated on the NiO_x film at 3,000 r.p.m. for 25 s and then annealed at 100 °C for 10 min. We opted to construct a NiO_x–Me–4PACz hole transport layer due to the well-documented ability of Me–4PACz to improve the photovoltaic performance of PSCs[34], while NiO_x acts to improving the wettability of perovskite on the self-assembled monolayer. Perovskite precursor solution (1.5 M, $Cs_{0.05}FA_{0.9}MA_{0.05}Pb(I_{0.95}Br_{0.05})_3$) was prepared by dissolving the PbI_2, $PbBr_2$, MABr, CsI, and FAI in a mixture of solvents DMF and DMSO at a volume ratio of 4:1. For the perovskite film fabrication, the substrate was spun at 2,000 r.p.m. for 35 s with an acceleration of 1,000 r.p.m. per second at first, and then at 7,000 r.p.m. for the 10 s with an acceleration of 7,000 r.p.m. per second. In the second step, 150 µl Anisole was dropped onto the substrate during the last 5 s of the spinning. The substrate was immediately placed on a hotplate and annealed at 100 °C for 10 min. For the posttreatment, the ligands were dissolved in IPA solution with concentration of 0.5 mg ml^{-1}, the surface treatment was finished by depositing 130 µl organic salts solution onto the perovskite film surface at a spin rate of 4,000 r.p.m. for 25 seconds with a 1,000-r.p.m. per second acceleration. The film was then annealed at 100 °C for 5 min to remove any residual IPA. After cooling to room temperature, the substrates were transferred to the evaporation system, 20 nm C_{60}, 8 nm BCP and 140 nm Ag were subsequently deposited by thermal evaporation. For PSCs used in MPP tracking, 8 nm of BCP was replaced with 20 nm of atomic-layer-deposited tin(IV) oxide (ALD-SnO_2) to limit environmentally induced degradation (Supplementary Note 8). Deposition of the ALD-SnO_2 was carried out using a PICOSUN R-200 Advanced ALD system. Water and tetrakis(dimethylamino)tin(IV) were used as the oxygen and tin precursors, respectively. The precursor and substrate temperature were set to 75 °C and 85 °C, respectively. Nitrogen gas (90 sccm) was used as carrier gas. The pulse and purge times for water were 1 s and 5 s, respectively, while for tetrakis(dimethylamino)tin(IV), they were 1.6 s and 5 s, respectively. The total number of cycles is 134, corresponding to 20 nm of SnO_2.

Device test

The current density–voltage (J–V) characteristics were measured using a Keithley 2400 source meter under illumination from a solar simulator (Newport, Class A) with a light intensity of 100 S5 mW cm^{-2} (checked with a calibrated reference solar cell from Newport). J–V curves were measured in a nitrogen atmosphere with a scanning rate of 100 mV s^{-1} (voltage step of 10 mV and delay time of 200 ms). The active area was determined by the aperture shade mask (0.049 cm^2 for small-area devices) placed in front of the solar cell. A spectral mismatch factor of 1 was used for all J–V measurements. We verified the effect of our champion passivator, ST, on the performance of PSCs at an independent third-party laboratory (Supplementary Note 9 and Supplementary Fig. 32).

Stability tests of solar cells

The stability tracking depicted in Fig. 5f is carried out under simulated 1-sun conditions utilizing a homemade white-light LED tracker. The intensity of the white-light LED tracker is calibrated to match 1-sun conditions. In contrast, the stability tracking in Supplementary Fig. 26 is conducted under AM1.5 G illumination, a multicolour LED solar simulator, with an illumination intensity of 100 mW cm^{-2}. The spectra of the LED simulators used in Fig. 5f and Supplementary Fig. 26 are presented in Supplementary Fig. 33 and Supplementary Fig. 34, respectively. In both setups, the device chamber was sealed and purged with nitrogen during room temperature tests (ISOS-L-1I) and MPP was monitored using a perturb and observe algorithm that updated the MPP point every 10 s. The devices were encapsulated by placing a glass slide on top and securing it with UV-adhesive (Lumtec LT-U001).

PLQY measurements and QFLS calculation

The excitation source was an unfocused beam of a 405 nm continuous-wave diode laser. Photoluminescence was collected using an integrating sphere with a precalibrated fibre coupled to a spectrometer (Ocean Optics QE Pro) with an intensity of ~100 mW cm^{-2}. PLQY values were calculated by PLQY = $P_S/(P_{Ex} \times A)$, where $A = 1 - P_L / P_{Ex}$, P_S is the integrated photon count of sample emission upon laser excitation; P_{Ex} is the integrated photon count of the excitation laser when the sample is removed from integrating sphere, and P_L is the integrated photon count of excitation laser when sample is mounted in the integrating sphere and hit by the beam. A set of neutral density filters were used to vary the excitation density to correspond to 1-sun illumination. QFLS is calculated by the PLQY values at various excitation light intensities, in this instance, just 1-sun excitation intensity was used: QFLS = $k_B T \times \ln(\text{PLQY} \times S \times J_G / J_{0,rad})$ where k_B is the Boltzmann constant, T is temperature, S is sun-equivalent excitation intensity, J_G the generated current density at 1 sun (taken from device J_{sc}) and $J_{0,rad}$ the radiative recombination current in the dark (taken from the dark current value from Shockley–Queisser limit). The detailed parameters for calculating QFLS from PLQY are provided in Supplementary Note 10.

XPS measurements

The high resolution XPS was performed by Nexsa G2 X-Ray Photoelectron Spectrometer System with a monochromated, micro-focused, and low-power Al K-Alpha X-ray source and an X-ray spot size of 200 um. The pass energy for the measurement is 50 eV. Vertical sputtering/profiling was performed using 1 keV Ar^+ ions (monatomic mode) with a raster size of 2 mm, resulting in a sputtering rate of roughly 0.57 nm s^{-1}. A single sputtering cycle lasted 10 seconds, at which point the sputtering crater was probed. This was repeated for a total of seven cycles.

Reporting summary

Further information on research design is available in the Nature Portfolio Reporting Summary linked to this article.

Data availability

The main data supporting the findings of this study are available within the Article and its Supplementary Information.

Code availability

We include the codes for the materials screening procedure in Supplementary Note 11 as well as the codes for preprocessing and ML model construction in Supplementary Note 12. The Vienna Ab initio Simulation Package code for the numerical simulations in this work can be found at https://www.vasp.at; the Gaussian code can be found at https://gaussian.com/; the Multiwfn code can be found at http://sobereva.com/multiwfn/; the scikit-learn is available at https://scikit-learn.org/; the Matplotlib is available at https://matplotlib.org.

References

24. Kresse, G. & Furthmüller, J. Efficient iterative schemes for ab initio total-energy calculations using a plane-wave basis set. *Phys. Rev. B* **54**, 11169–11186 (1996).
25. Perdew, J. P., Burke, K. & Ernzerhof, M. Generalized gradient approximation made simple. *Phys. Rev. Lett.* **77**, 3865–3868 (1996).
26. Heyd, J., Scuseria, G. E. & Ernzerhof, M. Hybrid functionals based on a screened Coulomb potential. *J. Chem. Phys.* **118**, 8207–8215 (2003).
27. Paier, J. et al. Screened hybrid density functionals applied to solids. *J. Chem. Phys.* **124**, 154709 (2006).
28. Lee, K., Murray, É. D., Kong, L., Lundqvist, B. I. & Langreth, D. C. Higher-accuracy van der Waals density functional. *Phys. Rev. B* **82**, 081101 (2010).
29. Maintz, S., Deringer, V. L., Tchougreeff, A. L. & Dronskowski, R. LOBSTER: a tool to extract chemical bonding from plane-wave based DFT. *J. Comput. Chem.* **37**, 1030–1035 (2016).
30. Henkelman, G., Uberuaga, B. P. & Jónsson, H. A climbing image nudged elastic band method for finding saddle points and minimum energy paths. *J. Chem. Phys.* **113**, 9901 (2000).
31. Lu, T. & Chen, F. Multiwfn: A multifunctional wavefunction analyzer. *J. Comput. Chem.* **33**, 580–592 (2012).
32. Guo, Y. et al. Machine-learning-guided discovery and optimization of additives in preparing Cu catalysts for CO2 reduction. *J. Am. Chem. Soc.* **143**, 5755–5762 (2021).
33. Chen, H. et al. Efficient and stable inverted perovskite solar cells incorporating secondary amines. *Adv. Mater.* **31**, e1903559 (2019).
34. Al-Ashouri, A. et al. Monolithic perovskite/silicon tandem solar cell with >29% efficiency by enhanced hole extraction. *Science* **370**, 1300–1309 (2020).

Acknowledgements

This research was made possible by King Abdullah University of Science and Technology Office of Sponsored Research under award no. OSR-2020-CRG9-4350.2 and by the US Department of the Navy, Office of Naval Research Grant (N00014-20-1-2572 (E.H.S.) and N00014-20-1-2725 (M.G.K.)). SciNet is funded by the Canada Foundation for Innovation under the auspices of Compute Canada. We thank W. Zhou for his contribution in independently verifying the impact of the ST treatment on PSC performance, under the supervision of Z. Ning from Shanghai Tech University.

Author contributions

J.X. conceived the idea. J.X., H.C., L.G. and E.H.S. designed the project. J.X. performed all DFT calculations and ML. H.C. fabricated the devices. L.G. and S.T. performed PL characterization. C.L. and Y.Y. carried out XPS, sputtering XPS and SEM characterization under the supervision of M.G.K. J.X. and Y.Y. analysed the XPS results. L.G. analysed the sputtering XPS and SEM results. A.M. fabricated the narrow-bandgap perovskite films. H.W. conducted the XRD measurement. S.M. and Y.C. participate in the ML aspect. J.X., L.G. and E.H.S. wrote the manuscript. B.C., B.R., S.M.P. and M.G.K. improved the manuscript. All authors discussed the results and commented on the paper.

Competing interests

The authors declare no competing interests.

Additional information

Supplementary information The online version contains supplementary material available at https://doi.org/10.1038/s41563-023-01705-y.

Correspondence and requests for materials should be addressed to Edward H. Sargent.

Peer review information *Nature Materials* thanks Jin Young Kim, Thierry Pauporte and Lei Zhang for their contribution to the peer review of this work.

nature portfolio

Corresponding author(s): Edward H. Sargent

Last updated by author(s): Sep 25, 2023

Reporting Summary

Nature Portfolio wishes to improve the reproducibility of the work that we publish. This form provides structure for consistency and transparency in reporting. For further information on Nature Portfolio policies, see our Editorial Policies and the Editorial Policy Checklist.

Statistics

For all statistical analyses, confirm that the following items are present in the figure legend, table legend, main text, or Methods section.

n/a	Confirmed
☐	☒ The exact sample size (*n*) for each experimental group/condition, given as a discrete number and unit of measurement
☐	☒ A statement on whether measurements were taken from distinct samples or whether the same sample was measured repeatedly
☐	☒ The statistical test(s) used AND whether they are one- or two-sided *Only common tests should be described solely by name; describe more complex techniques in the Methods section.*
☒	☐ A description of all covariates tested
☒	☐ A description of any assumptions or corrections, such as tests of normality and adjustment for multiple comparisons
☐	☒ A full description of the statistical parameters including central tendency (e.g. means) or other basic estimates (e.g. regression coefficient) AND variation (e.g. standard deviation) or associated estimates of uncertainty (e.g. confidence intervals)
☒	☐ For null hypothesis testing, the test statistic (e.g. *F*, *t*, *r*) with confidence intervals, effect sizes, degrees of freedom and *P* value noted *Give P values as exact values whenever suitable.*
☒	☐ For Bayesian analysis, information on the choice of priors and Markov chain Monte Carlo settings
☒	☐ For hierarchical and complex designs, identification of the appropriate level for tests and full reporting of outcomes
☒	☐ Estimates of effect sizes (e.g. Cohen's *d*, Pearson's *r*), indicating how they were calculated

Our web collection on statistics for biologists contains articles on many of the points above.

Software and code

Policy information about availability of computer code

Data collection	Supplementary Note 11
Data analysis	Supplementary Note 12

For manuscripts utilizing custom algorithms or software that are central to the research but not yet described in published literature, software must be made available to editors and reviewers. We strongly encourage code deposition in a community repository (e.g. GitHub). See the Nature Portfolio guidelines for submitting code & software for further information.

Data

Policy information about availability of data

All manuscripts must include a data availability statement. This statement should provide the following information, where applicable:

- Accession codes, unique identifiers, or web links for publicly available datasets
- A description of any restrictions on data availability
- For clinical datasets or third party data, please ensure that the statement adheres to our policy

The dataset used for machine learning is provided as a supplementary table.

Human research participants

Policy information about studies involving human research participants and Sex and Gender in Research.

Reporting on sex and gender	*Use the terms sex (biological attribute) and gender (shaped by social and cultural circumstances) carefully in order to avoid confusing both terms. Indicate if findings apply to only one sex or gender; describe whether sex and gender were considered in study design whether sex and/or gender was determined based on self-reporting or assigned and methods used. Provide in the source data disaggregated sex and gender data where this information has been collected, and consent has been obtained for sharing of individual-level data; provide overall numbers in this Reporting Summary. Please state if this information has not been collected. Report sex- and gender-based analyses where performed, justify reasons for lack of sex- and gender-based analysis.*
Population characteristics	*Describe the covariate-relevant population characteristics of the human research participants (e.g. age, genotypic information, past and current diagnosis and treatment categories). If you filled out the behavioural & social sciences study design questions and have nothing to add here, write "See above."*
Recruitment	*Describe how participants were recruited. Outline any potential self-selection bias or other biases that may be present and how these are likely to impact results.*
Ethics oversight	*Identify the organization(s) that approved the study protocol.*

Note that full information on the approval of the study protocol must also be provided in the manuscript.

Field-specific reporting

Please select the one below that is the best fit for your research. If you are not sure, read the appropriate sections before making your selection.

☐ Life sciences ☐ Behavioural & social sciences ☐ Ecological, evolutionary & environmental sciences

For a reference copy of the document with all sections, see nature.com/documents/nr-reporting-summary-flat.pdf

Life sciences study design

All studies must disclose on these points even when the disclosure is negative.

Sample size	*Describe how sample size was determined, detailing any statistical methods used to predetermine sample size OR if no sample-size calculation was performed, describe how sample sizes were chosen and provide a rationale for why these sample sizes are sufficient.*
Data exclusions	*Describe any data exclusions. If no data were excluded from the analyses, state so OR if data were excluded, describe the exclusions and the rationale behind them, indicating whether exclusion criteria were pre-established.*
Replication	*Describe the measures taken to verify the reproducibility of the experimental findings. If all attempts at replication were successful, confirm this OR if there are any findings that were not replicated or cannot be reproduced, note this and describe why.*
Randomization	*Describe how samples/organisms/participants were allocated into experimental groups. If allocation was not random, describe how covariates were controlled OR if this is not relevant to your study, explain why.*
Blinding	*Describe whether the investigators were blinded to group allocation during data collection and/or analysis. If blinding was not possible, describe why OR explain why blinding was not relevant to your study.*

Behavioural & social sciences study design

All studies must disclose on these points even when the disclosure is negative.

Study description	*Briefly describe the study type including whether data are quantitative, qualitative, or mixed-methods (e.g. qualitative cross-sectional, quantitative experimental, mixed-methods case study).*
Research sample	*State the research sample (e.g. Harvard university undergraduates, villagers in rural India) and provide relevant demographic information (e.g. age, sex) and indicate whether the sample is representative. Provide a rationale for the study sample chosen. For studies involving existing datasets, please describe the dataset and source.*
Sampling strategy	*Describe the sampling procedure (e.g. random, snowball, stratified, convenience). Describe the statistical methods that were used to predetermine sample size OR if no sample-size calculation was performed, describe how sample sizes were chosen and provide a rationale for why these sample sizes are sufficient. For qualitative data, please indicate whether data saturation was considered, and what criteria were used to decide that no further sampling was needed.*

Data collection	*Provide details about the data collection procedure, including the instruments or devices used to record the data (e.g. pen and paper, computer, eye tracker, video or audio equipment) whether anyone was present besides the participant(s) and the researcher, and whether the researcher was blind to experimental condition and/or the study hypothesis during data collection.*
Timing	*Indicate the start and stop dates of data collection. If there is a gap between collection periods, state the dates for each sample cohort.*
Data exclusions	*If no data were excluded from the analyses, state so OR if data were excluded, provide the exact number of exclusions and the rationale behind them, indicating whether exclusion criteria were pre-established.*
Non-participation	*State how many participants dropped out/declined participation and the reason(s) given OR provide response rate OR state that no participants dropped out/declined participation.*
Randomization	*If participants were not allocated into experimental groups, state so OR describe how participants were allocated to groups, and if allocation was not random, describe how covariates were controlled.*

Ecological, evolutionary & environmental sciences study design

All studies must disclose on these points even when the disclosure is negative.

Study description	*Briefly describe the study. For quantitative data include treatment factors and interactions, design structure (e.g. factorial, nested, hierarchical), nature and number of experimental units and replicates.*
Research sample	*Describe the research sample (e.g. a group of tagged Passer domesticus, all Stenocereus thurberi within Organ Pipe Cactus National Monument), and provide a rationale for the sample choice. When relevant, describe the organism taxa, source, sex, age range and any manipulations. State what population the sample is meant to represent when applicable. For studies involving existing datasets, describe the data and its source.*
Sampling strategy	*Note the sampling procedure. Describe the statistical methods that were used to predetermine sample size OR if no sample-size calculation was performed, describe how sample sizes were chosen and provide a rationale for why these sample sizes are sufficient.*
Data collection	*Describe the data collection procedure, including who recorded the data and how.*
Timing and spatial scale	*Indicate the start and stop dates of data collection, noting the frequency and periodicity of sampling and providing a rationale for these choices. If there is a gap between collection periods, state the dates for each sample cohort. Specify the spatial scale from which the data are taken*
Data exclusions	*If no data were excluded from the analyses, state so OR if data were excluded, describe the exclusions and the rationale behind them, indicating whether exclusion criteria were pre-established.*
Reproducibility	*Describe the measures taken to verify the reproducibility of experimental findings. For each experiment, note whether any attempts to repeat the experiment failed OR state that all attempts to repeat the experiment were successful.*
Randomization	*Describe how samples/organisms/participants were allocated into groups. If allocation was not random, describe how covariates were controlled. If this is not relevant to your study, explain why.*
Blinding	*Describe the extent of blinding used during data acquisition and analysis. If blinding was not possible, describe why OR explain why blinding was not relevant to your study.*

Did the study involve field work? ☐ Yes ☒ No

Reporting for specific materials, systems and methods

We require information from authors about some types of materials, experimental systems and methods used in many studies. Here, indicate whether each material, system or method listed is relevant to your study. If you are not sure if a list item applies to your research, read the appropriate section before selecting a response.

Materials & experimental systems

n/a	Involved in the study
☒	☐ Antibodies
☒	☐ Eukaryotic cell lines
☒	☐ Palaeontology and archaeology
☒	☐ Animals and other organisms
☒	☐ Clinical data
☒	☐ Dual use research of concern

Methods

n/a	Involved in the study
☒	☐ ChIP-seq
☒	☐ Flow cytometry
☒	☐ MRI-based neuroimaging